

Article

# Nonlinear Vibration of Cracked Porous FG-GPL RC Cylindrical Panels Using a Phase-Field Crack Model

Jin-Rae Cho 

Department of Naval Architecture and Ocean Engineering, Hongik University, Jochiwon, Sejong 30016, Republic of Korea; jrcho@hongik.ac.kr; Tel.: +82-44-860-2546

**Featured Application:** Novel design of functionally graded graphene nanocomposite structures.

**Abstract:** This study is concerned with the nonlinear free vibration of a cracked functionally graded porous cylindrical panel reinforced with graphene platelets by introducing a phase-field crack model. Conventional crack modeling by separating the grid nodes lying on the crack line is not only painstaking but also suffers from numerical instability. To overcome this problem, the internal crack is modeled by adopting the phase-field formulation and a virtual geometry rotation. The nonlinear numerical method is developed based on the first-order shear deformation theory incorporated with the von Kármán geometry nonlinearity in the framework of the 2-D extended natural element method, a recently introduced mesh-free method. The crack-induced singular field is represented by adopting the crack-tip singular functions, and the troublesome numerical locking is restrained by combining the MITC3+ shell concept and the shear stabilization factor. The curved shell surface is mapped to a 2-D rectangular NEM grid to avoid difficulty in defining the interpolation functions. The developed numerical method is verified through a comparison with the reference solutions, and the large-amplitude free vibration of porous cracked functionally graded graphene platelet-reinforced cylindrical panels is profoundly examined by changing the major parameters.

**Keywords:** functionally graded; GPL-reinforced composite; porous cracked cylindrical panel; nonlinear free vibration; 2-D extended NEM; shear stabilization



**Citation:** Cho, J.-R. Nonlinear Vibration of Cracked Porous FG-GPL RC Cylindrical Panels Using a Phase-Field Crack Model. *Appl. Sci.* **2024**, *14*, 4281. <https://doi.org/10.3390/app14104281>

Academic Editors: Magdalena Palacz and Marek Krawczuk

Received: 21 April 2024

Revised: 15 May 2024

Accepted: 15 May 2024

Published: 18 May 2024



**Copyright:** © 2024 by the author. Licensee MDPI, Basel, Switzerland. This article is an open access article distributed under the terms and conditions of the Creative Commons Attribution (CC BY) license (<https://creativecommons.org/licenses/by/4.0/>).

## 1. Introduction

Currently, nanocomposites in which nanofillers such as graphene platelets (GPLs) or carbon nanotubes (CNTs) are reinforced have been attracting much attention [1,2]. These nanofillers exhibit excellent physical, chemical, and electrical properties so that their introduction can dramatically improve the performances of conventional composites. It was reported that the structural strength of polymeric composites is greatly increased when only a tiny amount of nanofillers are reinforced [3]. In terms of application, the nanocomposites are manufactured in the form of beams, plates, and shells, and their basic mechanical behaviors such as static deflection, free vibration, and buckling have been intensively and continuously investigated [4–6]. This is because the quantitative investigation of their mechanical responses is needed for their practical design in the specific configuration under consideration, even though the superiority of material graphene has been qualitatively well-known. The mechanical behaviors of these nanocomposites are strongly affected by the distribution patterns of nanofillers, particularly through the thickness of the composite structures. So, several purposeful thickness-wise distribution patterns have been proposed according to the notion of functionally graded material (FGM), which was introduced in the late 1990s to overcome bi-material-type heat-proof composites [7–10]. The representative functional distributions are FG-U, FG-O, FG-X, and FG- $\wedge$ , and the nanocomposite structures with these functional distributions of nanofillers are called FG-GPLRC and FG-CNTRC structures.

Besides the functional distribution of nanofillers, the mechanical behaviors of functional nanocomposite structures are affected by the porosity distribution. This is because the difference in the solidification temperatures of a matrix and a filler during fabrication produces porosities [11,12], and both the stiffness and mass of composite structure are remarkably influenced by the amount and distribution pattern of porosity. In this context, recently, porosity has been widely taken into consideration in the parametric investigation of the mechanical behaviors of functional nanocomposites with respect to the porosity coefficient and distribution [13–15]. Moreover, the combination of nanofiller and porosity distribution patterns leads to more diverse mechanical behaviors of functional nanocomposites because both distribution patterns are usually not the same as one another. Due to their excellent material properties and the low density, functionally graded porous nanocomposites have been attracting much attention for high-strength, lightweight structures [16].

Carbon nanotubes are cylindrical in form so their production costs are relatively higher than that of graphene platelets. In addition, their material properties are not isotropic but orthotropic, with a higher elastic modulus in the direction of CNT alignment. Thus, the mechanical responses of FG-CNTRC structures are sensitive to the CNT alignment direction such that those in the two off-alignment directions are worse than those of FG-GPLRC structures [17–19]. On the other hand, FG-GPLRC structures are usually modeled as isotropic materials according to the micromechanical homogenization approach [20]. For this reason, together with their relatively low production costs, FG-GPLRC structures nowadays are attracting more attention [18]. Meanwhile, the studies on FG-GPLRC have been based on those of FG-CNTRC because GPLs received attention somewhat later than CNTs. As well, studies on the fundamental mechanical responses of FG-GPLRC structures have mostly included geometry nonlinearity in the displacement field according to the increase in interest on large deflection bending and large amplitude vibration.

Regarding studies on the nonlinear free vibration of GPL-reinforced structures, Feng et al. [21] studied the nonlinear free vibration of a multi-layer polymer composite beam reinforced with non-uniformly distributed GPLs through the thickness by applying Hamilton's principle and the von Kármán nonlinearity to Timoshenko beam theory. Zhang et al. [22] numerically examined the nonlinear vibration of graphene sheets by applying the element-free kp-Ritz method to the nonlocal elasticity theory, which accounts for the size effect. Gao et al. [23] numerically examined the influence of GPL and porosity distributions on the nonlinear natural vibration of FG-GPLRC porous plates supported by the elastic foundations by applying the differential quadrature method (DQM). Shen et al. [24] investigated the temperature-dependent large amplitude vibration of GPLRC-laminated cylindrical panels resting on an elastic foundation using a two-step perturbation technique. Kiani [25] proposed a nonlinear formulation for the nonlinear natural vibration of GPLRC-laminated plates using a non-uniform rational B-spline (NURBS)-based isogeometric finite element method. Teng and Wang [26] analytically investigated the influence of porosity coefficient and the foam skeleton distribution on the nonlinear free vibration of graphene-reinforced plates by applying Hamilton's principle to the von Kármán nonlinear plate theory. Song et al. [27] numerically and parametrically investigated the temperature-dependent nonlinear free vibration characteristics of the cracked FG-GPLRC beams resting on an elastic foundation using the DQM. Tao and Dai [28] analyzed the size-dependent nonlinear free vibration of FG-GPLRC annular sector microplates by applying the isogeometric analysis to a four-variable higher-order SDT. Javani et al. [29] investigated the nonlinear natural vibration of an FG-GPLRC circular plate on the nonlinear elastic foundation using the generalized DQM. Wang and Chen [30] numerically investigated the nonlinear natural vibration of an FG-GPLRC titanium alloy trapezoid plate using the Rayleigh–Ritz method and the direct iterative process.

As can be found from the literature survey, previous studies on the nonlinear free vibration of FG-GPLRC structures were mostly limited to beams and plates and furthermore assumed that the structures are perfect without any cracks. However, the structural

elements used in real applications have various forms such as cylindrical and conical shells, and various abnormal loading conditions such as thermal shock may induce micro-cracking [31] within GPL-reinforced nanocomposite structures. These undesired cracks damage the surrounding region such that the whole structural strength becomes significantly weakened, implying that the consideration of a crack is essential in structural analyses and designs. Meanwhile, the consideration of a crack in a mesh- or grid-based numerical analysis may frequently suffer from the painstaking crack modeling job [32–34]. Furthermore, the crack modeling deteriorates the mesh uniformity, which may induce numerical instability and even numerical failure.

In this situation, this study aims to determine the large amplitude natural vibration of a porous FG-GPLRC cylindrical panel with a central inclined crack. To avoid the above-mentioned problems in crack meshing, the phase field formulation (PFF) [35,36] is adopted and a virtual geometry rotation is introduced into the framework of 2-D extended NEM [19,37]. In other words, the nodes sitting on the crack lines are not separated and the region at the crack-tip in the grid is not centrally refined. Instead, the crack line is represented by the phase field and its virtual rotation to the NEM grid line, and the crack-induced singularity is enhanced by the near-tip singular functions [38]. The large displacement field is expressed by the first-order SDT incorporated with the von Kármán geometry nonlinearity. The painstaking definition and manipulation of high-smooth Laplace interpolation (L/I) functions in NEM is relaxed by mapping the cylindrical neutral surface to a rectangular plane. And, the troublesome numerical locking [39,40] is restrained by adopting the MITC3+ shell concept and the shear stabilization factor. In the MITC3+ shell concept, the transverse shear strains are re-interpolated at six tying points within a three-node triangular shell element to suppress shear locking [41]. The developed nonlinear vibration method is justified through the comparison with the reference solutions. And, the nonlinear natural vibration characteristics of porous FG-GPLRC cylindrical panels are profoundly investigated by changing the major parameters of GPLs and porosity and by combining the GPL and porosity distributions. Furthermore, a comparison with FG-CNTRC cylindrical panels is also presented.

## 2. Functionally Graded Porous GPLRC Cylindrical Panel

Figure 1a represents a cylindrical panel in which GPLs are distributed with a specific distribution pattern through the thickness. Cartesian coordinates  $(x, y, z)$  are introduced on the corner of the neutral surface  $\varpi$  of the panel with the  $x$ -axis along the cylinder axis and the  $z$ -axis through the thickness. The radial distance between the neutral surface and the mid-surface is denoted by  $e$  [42]. The geometry of cylindrical panel is characterized by length  $L$ , radius  $R$ , sub-tended angle  $\theta_0$ , and uniform thickness  $h$ . Then, the material domain  $\Omega \in \mathfrak{R}^3$  can be expressed by  $\Omega = \varpi \times [-h/2, h/2]$ . Four thickness-wise functional distribution patterns of GPLs are depicted in Figure 1b—FG-U, FG-O, FG-X, and FG- $\Lambda$ —where the GPLs are uniform in FG-U, biased towards the neutral surface in FG-O, concentrated in the top and bottom regions in FG-X, and biased towards the bottom in FG- $\Lambda$ . In addition, pores and a central crack are included within the panel, as will be described below.

The thickness-wise volume fractions of the GPLs and the underlying matrix are denoted by  $f_{GPL}(z)$  and  $f_m(z)$ . Then, either one is enough to identify both volume fractions as two volume fractions satisfy the physical constraint given by

$$f_{GPL}(z) + f_m(z) = 1 \quad (1)$$

The GPL volume fraction  $f_{GPL}(z)$  is chosen in this study and its mathematical expression becomes

$$f_{GPL}(z) = \begin{cases} V_{GPL}^* & \text{FG - U} \\ 2(1 - 2|z|/h)V_{GPL}^* & \text{FG - O} \\ 2(2|z|/h)V_{GPL}^* & \text{FG - X} \\ (1 - 2z/h)V_{GPL}^* & \text{FG - } \Lambda \end{cases} \quad (2)$$

depending on the GPL distribution pattern, where the total GPL volume fraction  $V_{GPL}^*$  is calculated by

$$V_{GPL}^* = \frac{g_{GPL}}{g_{GPL} + \rho_{GPL}(1 - g_{GPL})/\rho_m} \quad (3)$$

using the GPL mass fraction  $g_{GPL}^*$ , and the two densities  $\rho_{GPL}$  and  $\rho_m$  of the GPL and matrix material.

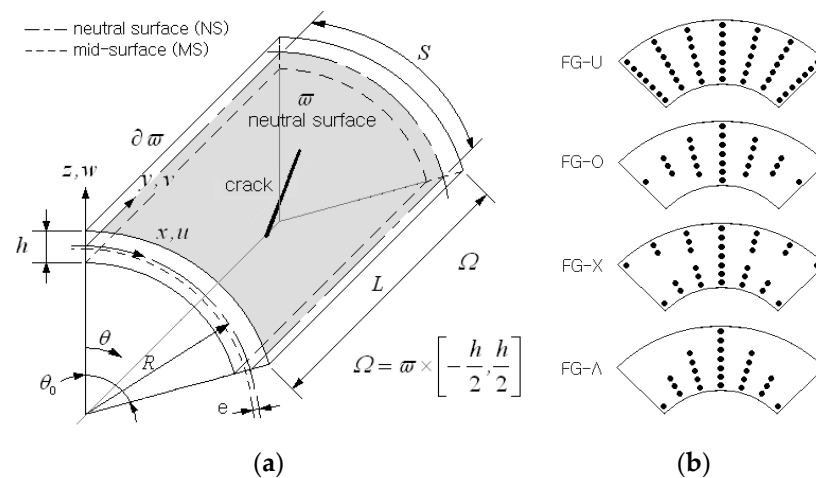


**Figure 1.** A cylindrical panel reinforced with graphene platelets: (a) geometry and dimensions, and (b) GPL distribution patterns.

GPLs are modeled as a rectangular solid with length  $l_{GPL}$ , width  $w_{GPL}$ , and thickness  $t_{GPL}$ , and their distribution is assumed to be uniform within the underlying matrix in the local sense. So, the graphene-reinforced composites are usually considered isotropic and their effective Young’s modulus  $E_C$  is evaluated using the Halphin-Tsai approach [20]:

$$E_C = \frac{3}{8} \cdot \frac{1 + \zeta_L \eta_L f_{GPL}}{1 - \eta_L f_{GPL}} E_m + \frac{5}{8} \cdot \frac{1 + \zeta_T \eta_T f_{GPL}}{1 - \eta_T f_{GPL}} E_m \quad (4)$$

with

$$\eta_L = \frac{E_{GPL} - E_m}{E_{GPL} + \zeta_L E_m}, \quad \eta_T = \frac{E_{GPL} - E_m}{E_{GPL} + \zeta_T E_m} \quad (5)$$

in which  $E_{GPL}$  and  $E_m$  are the elastic moduli of GPLs and matrix material, and the relative geometry ratios  $\zeta_L$  and  $\zeta_T$  are defined by

$$\zeta_L = \frac{2l_{GPL}}{t_{GPL}}, \quad \zeta_T = \frac{2w_{GPL}}{t_{GPL}} \quad (6)$$

In a similar manner, the effective values of mass density  $\rho_C$  and Poisson’s ratio  $\nu_C$  of GPLRC are determined by

$$\rho_C = V_{GPL} \rho_{GPL} + V_m \rho_m \quad (7)$$

$$\nu_C = V_{GPL} \nu_{GPL} + V_m \nu_m \quad (8)$$

using the simplest linear rule of mixture.

The porosity within GPLRC is generally characterized by size, shape, orientation, and dispersion structure of pores. In this study, the former three factors are assumed to be uniform in space, but only the relative volume of pore and the dispersion structure are considered for the parametric investigation of pores. Figure 2 shows three different porosity distributions considered in this study, center-biased (PD\_1), outer-biased (PD\_2), and uniform (PD\_3), which are expressed as

$$PD_1 : \chi(z) = e_0 \cdot \cos\left(\frac{\pi z}{h}\right) \tag{9}$$

$$PD_2 : \chi(z) = e_0 \cdot \left(\cos\left|\frac{\pi z}{h}\right| - \frac{\pi}{2}\right) \tag{10}$$

$$PD_3 : \chi(z) = e_0 \tag{11}$$

where  $e_0 (0 \leq e_0 \leq 1)$  denotes the porosity coefficient, which is related to the relative volumes of pores within GPLRC.

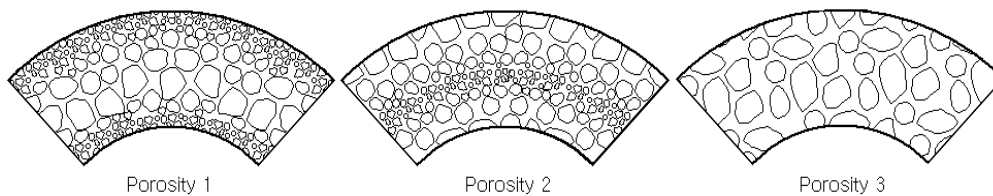


**Figure 2.** Three porosity distributions (PD\_1: center-biased, PD\_2: outer-biased, and PD\_3: uniform).

The porosity affects the effective material properties of GPLRC so that the above elastic modulus  $E_C$ , shear modulus  $G_C = E_C/2(1 + \nu_C)$ , and mass density  $\rho_C$  should be corrected. Denoting the effective material properties before and after modification by  $\wp_C(z)$  and  $\wp(z)$ , the modification is made through

$$\wp(z) = \wp_C(z) \cdot [1 - \chi(z)] \tag{12}$$

except for the mass density. For the effective mass density, the porosity coefficient  $e_0$  should be corrected using the relationship given by

$$\left[\frac{\rho(z)}{\rho_C(z)}\right]^2 = \frac{E(z)}{E_C(z)} \tag{13}$$

between the mass density and elastic property [43]. Then, the corrected porosity coefficient  $e_m$  for the mass density is determined by

$$1 - e_m \cdot \cos\left(\frac{\pi z}{h}\right) = \sqrt{1 - e_0 \cdot \cos(\pi z/h)} \tag{14}$$

for porosity distribution PD\_1, for example.

Figure 3 represents a central crack within a cylindrical panel, which is characterized by the inclination angle  $\alpha$  and the length  $a$ . The crack center coincides with the center of the cylindrical panel, and these two parameters are taken as variables for the parametric experiment. The polar coordinates are added to two crack tips in order to express the singular functions the are needed to capture the singularity at the crack tips. The existence of a crack can be determined by either creating a crack line or employing the phase field concept [35] without creating a crack line. The former is usually implemented by separating the nodes sitting on the crack line in FEM or NEM grids [2]. But, the node separation in the former approach not only is painstaking but also produces a non-uniform distorted grid, which may deteriorate the numerical accuracy or even lead to numerical failure. This difficulty becomes more severe in the crack propagation simulation for which tedious crack tracking is essential [35].

On the other hand, the latter approach employs an additional state variable called phase field  $\phi(x)$  ( $0 \leq \phi \leq 1$ ). The value of  $\phi(x)$  indicates the damage state at point  $x$  within the structure such that  $\phi = 1$  indicates fully damaged while  $\phi = 0$  denotes completely undamaged. This method does not need the painstaking crack mesh generation, which can significantly reduce the troublesome mesh adaptation job in crack propagation simulation to track the crack. In addition, there is no need to assume material homogeneity and isotropy regions away from the crack. Thus, there exist no limitations in the material type for the phase field formulation. But, it needs an extra approximation of the phase field to represent the existence of a crack within the material domain. The crack line is modeled by connecting the points with  $\phi = 1$ , and the transition region [35] between the fully damage crack line and the completely undamaged region has the value of  $0 < \phi < 1$ . The size of the transient region is denoted by the length scale [44,45], which is controlled by the grid density near the crack line when the phase field is approximated using the same grid constructed for the displacement field approximation.

According to this concept, the total strain energy  $U$  and the total kinetic energy  $T$  of cracked structure are expressed as

$$U = \int_{\Omega} (1 - \phi)^2 \hat{U} dV \tag{15}$$

$$T = \int_{\Omega} (1 - \phi)^2 \hat{T} dV \tag{16}$$

where  $\hat{U}$  and  $\hat{T}$  denote the total strain and total kinetic energies when the structure is completely undamaged.

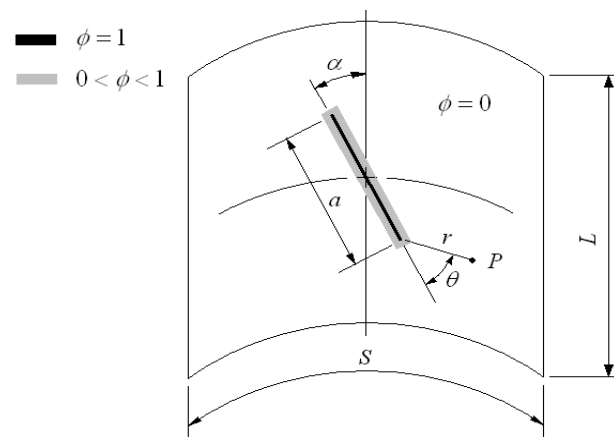


Figure 3. A central crack and phase field  $\phi(x)$  within a cylindrical panel.

Letting  $\mathbf{d} = (u_0, v_0, w_0, \beta_x, \beta_y)^T$  be the displacement vector, the displacement field  $\mathbf{u} = \{u, v, w\}^T$  of FG-GPLRC cylindrical panel is expressed as

$$\begin{Bmatrix} u \\ v \\ w \end{Bmatrix}_{(x,y,z)} = \begin{Bmatrix} u_0 \\ v_0 \\ w_0 \end{Bmatrix}_{(x,y)} + z \cdot \begin{Bmatrix} \beta_x \\ \beta_y \\ 0 \end{Bmatrix}_{(x,y)} \tag{17}$$

according to the FSDT. The large deflection of a cylindrical panel is represented by the von Kármán nonlinearity, which leads to the strain-displacement relations given by

$$\boldsymbol{\varepsilon} = \left\{ \begin{array}{l} \frac{w_0}{r} + \frac{\partial u_0}{\partial x} + \frac{1}{2} \tilde{w},_x \frac{\partial w}{\partial x} \\ \frac{\partial v_0}{\partial y} + \frac{1}{2} \tilde{w},_y \frac{\partial w}{\partial y} \\ \frac{\partial v_0}{\partial x} + \frac{\partial u_0}{\partial y} + \frac{1}{2} (\tilde{w},_x \frac{\partial w}{\partial x} + \tilde{w},_y \frac{\partial w}{\partial y}) \end{array} \right\} + z \cdot \left\{ \begin{array}{l} \frac{\partial \beta_x}{\partial x} \\ \frac{\partial \beta_y}{\partial y} \\ \frac{\partial \beta_x}{\partial y} + \frac{\partial \beta_y}{\partial x} \end{array} \right\} = (\mathbf{H}_L + \mathbf{H}_{NL}) \mathbf{d} \tag{18}$$

$$\gamma = \left\{ \begin{array}{c} \beta_y + \frac{\partial w_0}{\partial y} \\ \beta_x + \frac{\partial w_0}{\partial x} - \frac{u_0}{r} \end{array} \right\} = \mathbf{H}_s \mathbf{d} \tag{19}$$

with  $\varepsilon = \{\varepsilon_{xx}, \varepsilon_{yy}, 2\varepsilon_{xy}\}^T$ ,  $\gamma = \{\gamma_{yz}, \gamma_{zx}\}^T$ , and  $r = R + z \approx R$ , where  $\mathbf{H}_L$ ,  $\mathbf{H}_{NL}$ , and  $\mathbf{H}_s$  denote the  $(3 \times 5)$  and  $(2 \times 5)$  partial derivative matrices defined by

$$\mathbf{H}_L = \begin{bmatrix} H_x & 0 & 1/r & z \cdot H_x & 0 \\ 0 & H_y & 0 & 0 & z \cdot H_y \\ H_y & H_x & 0 & z \cdot H_y & z \cdot H_x \end{bmatrix} \tag{20}$$

$$\mathbf{H}_{NL} = \begin{bmatrix} 0 & 0 & \tilde{w}_{,x} H_x / 2 & 0 & 0 \\ 0 & 0 & \tilde{w}_{,y} H_y / 2 & 0 & 0 \\ 0 & 0 & (\tilde{w}_{,x} H_y + \tilde{w}_{,y} H_x) / 2 & 0 & 0 \end{bmatrix} \tag{21}$$

$$\mathbf{H}_s = \begin{bmatrix} 0 & 0 & H_y & 0 & 1 \\ -1/r & 0 & H_x & 1 & 0 \end{bmatrix} \tag{22}$$

with  $H_x = \partial/\partial x$  and  $H_y = \partial/\partial y$ . Here,  $\tilde{w}_{,x}$  and  $\tilde{w}_{,y}$  are the deflection derivatives of a panel, which are assumed to be known a priori, as described later. Then, the strain–stress constitutive relations become

$$\sigma = \frac{E_C}{1 - \nu_C^2} \begin{bmatrix} 1 & \nu_C & 0 \\ \nu_C & 1 & 0 \\ 0 & 0 & (1 - \nu_C)/2 \end{bmatrix} \left\{ \begin{array}{c} \varepsilon_{xx} \\ \varepsilon_{yy} \\ 2\varepsilon_{xy} \end{array} \right\} = \mathbf{D}(\mathbf{H}_L + \mathbf{H}_{NL}) \mathbf{d} \tag{23}$$

$$\tau = \begin{bmatrix} G_C & 0 \\ 0 & G_C \end{bmatrix} \left\{ \begin{array}{c} \gamma_{yz} \\ \gamma_{zx} \end{array} \right\} = \mathbf{D}_s \mathbf{H}_s \mathbf{d} \tag{24}$$

with  $\sigma = \{\sigma_{xx}, \sigma_{yy}, \sigma_{xy}\}^T$  and  $\tau = \{\tau_{yz}, \tau_{zx}\}^T$ .

### 3. NE Approximation of Nonlinear Natural Vibration Using Phase-Field Crack Model

Referring to Figure 4, the panel neutral surface  $\omega$  is uniformly divided into a finite number of three-node Delaunay triangles. As mentioned above, the crack line is modeled using the phase field  $\phi(x)$  and the crack-induced singular field is represented by adding the crack-tip singular functions without refining the local NEM grid in the vicinity of crack tip. Thus, in an extended NEM, the displacement  $\mathbf{u}(x, y, z)$  is approximated as

$$\mathbf{u}^h(\mathbf{x}) = \sum_{J=1}^N (\mathbf{r}_J + z \mathbf{d}_J) \Psi_J(x, y) + \sum_{I=1}^2 \sum_{k=1}^4 (\hat{\mathbf{r}}_I^k + z \hat{\mathbf{d}}_I^k) \left\{ \begin{array}{c} Q_I^k(r, \theta) \\ Q_I^k(r, \theta) \\ R_I^k(r, \theta) \end{array} \right\} \tag{25}$$

using the L/I functions  $\psi_J(x, y)$  [46,47] and the crack-tip singular functions  $Q_k(r, \theta)$  and  $R_k(r, \theta)$  [38].

$$\left\{ Q_I^k(r, \theta) \right\} = \left\{ \sqrt{r} \sin\left(\frac{\theta}{2}\right), \sqrt{r} \cos\left(\frac{\theta}{2}\right), \sqrt{r} \sin\left(\frac{\theta}{2}\right) \sin(\theta), \sqrt{r} \cos\left(\frac{\theta}{2}\right) \sin(\theta) \right\} \tag{26}$$

$$\left\{ R_I^k(r, \theta) \right\} = \left\{ \sqrt{r} \sin\left(\frac{\theta}{2}\right), 0, 0, 0 \right\} \tag{27}$$

The singular functions are defined using two distinct crack-tip polar coordinates  $(r, \theta)_I (I = 1, 2)$ , as depicted in Figure 3. Here,  $\mathbf{b}_J = (\mathbf{r}_J, \mathbf{d}_J)$  are the non-singular nodal displacement vectors at node  $J$  within the NEM grid  $\mathfrak{S}_C$  generated with  $N$  nodes and  $M$

Delaunay triangles. And,  $s_I^k = (\hat{r}_I^k, \hat{d}_I^k)$  indicates the singular vector corresponding to the  $k$ -th singular function.

The derivation and manipulation of L/I functions on the curved cylindrical surfaces are troublesome, so the physical NEM grid  $\mathfrak{S}_C = [0, S] \times [0, L]$  on the panel neutral surface is transformed into 2-D rectangular NEM grid  $\mathfrak{S}_R = [0, \theta_0] \times [0, L]$  for the computation. Then, according to the geometry transformation  $T_C$  and the chain rule summarized in Appendix A, the enriched NE approximation of the bending-membrane strain  $\varepsilon$  in Equation (18) and the transverse shear (T/S) strain  $\gamma$  in Equation (19) ends up with

$$\varepsilon^h = \sum_{J=1}^N \tilde{L}\phi_J \mathbf{b}_J + \sum_{I=1}^2 \sum_{k=1}^4 L \Phi_I^k s_I^k = \sum_{J=1}^N \mathbf{B}_J \mathbf{b}_J + \sum_{I=1}^2 \sum_{k=1}^4 \mathbf{H}_{sI}^k s_I^k \tag{28}$$

$$\gamma^h = \sum_{J=1}^N \tilde{L}_s \phi_J \mathbf{b}_J + \sum_{I=1}^2 \sum_{k=1}^4 L_s \Phi_I^k s_I^k = \sum_{J=1}^N \mathbf{B}_s^J \mathbf{b}_J + \sum_{I=1}^2 \sum_{k=1}^4 \mathbf{H}_{sI}^k s_I^k \tag{29}$$

with  $\Phi_I^k = \{Q_I^k, Q_I^k, R_I^k\}$ . Here,  $\mathbf{B}_J = \tilde{L}\phi_J$  is computed on the 2-D rectangular NEM grid while  $\mathbf{H}_{sI}^k = L\Phi_I^k$  is computed directly on the panel neutral surface (Similarly for  $\mathbf{B}_s^J$  and  $\mathbf{H}_{sI}^k$ ).

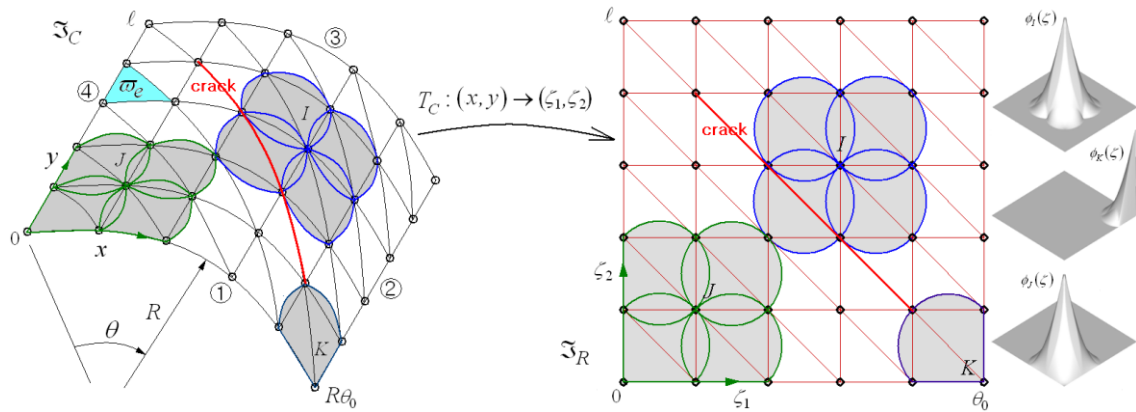


**Figure 4.** A geometry transformation  $T_C$  between the curved and planar NEM grids and L/I functions  $\phi_J(\zeta_1, \zeta_2)$  defined on a 2-D rectangular plane.

Note that the first term on the right-hand side in Equation (29), which is approximated with  $C^0$ -L/I functions  $\phi_J$ , may suffer from numerical locking when the deformation is bending-dominated [39,40]. This problem can be effectively suppressed by indirectly interpolating this non-singular term of T/S strain according to the MITC3+ shell approach [41], as addressed in Appendix B. The analytical calculation of Equations (A5) and (A6) in Appendix B using Equations (19) and (22), together with the chain rule between two coordinates  $(x, y)$  and  $(\zeta, \eta)$  in Figure 4, results in

$$\gamma_e^h = \hat{\mathbf{B}}_e \mathbf{b}_e \tag{30}$$

Here,  $\hat{\mathbf{B}}_e$  is the  $(2 \times 15)$  triangle-wise matrices in function of  $\zeta, \eta, z$ , and  $R$ , and  $\mathbf{b}_e = \{\mathbf{b}_1^e, \mathbf{b}_2^e, \mathbf{b}_3^e\}$  are the  $(15 \times 1)$  non-singular triangle-wise nodal vectors.

Next, the nonlinear vibration of the FG-GPLRC cylindrical panel is governed by the dynamic form of the energy principle given by

$$\delta U + \delta T = 0 \tag{31}$$



where  $\omega_I$  and  $\bar{\mathbf{d}}_I = [\mathbf{d}_1, \mathbf{d}_2, \dots, \mathbf{d}_N]_I$  denote the nonlinear natural frequencies and natural modes, and two linear and one nonlinear stiffness matrix and the mass matrix are calculated as

$$\mathbf{K}_{L,\sigma} = \int_{-h/2+e}^{h/2-e} \int_{\omega} (1 - \phi)^2 \mathbf{B}_L^T \mathbf{D} \mathbf{B}_L d\omega dz \tag{38}$$

$$\mathbf{K}_{L,s}^e = \int_{-h/2+e}^{h/2-e} \int_{\omega_e} (1 - \phi)^2 \hat{\mathbf{B}}_e^T \hat{\mathbf{D}}_s \hat{\mathbf{B}}_e d\omega dz \tag{39}$$

$$\mathbf{K}_{NL} = \int_{-h/2+e}^{h/2-e} \int_{\omega} (1 - \phi)^2 \left[ \mathbf{B}_L^T \mathbf{D} \mathbf{B}_{NL} + \mathbf{B}_{NL}^T \mathbf{D} \mathbf{B}_L + \mathbf{B}_{NL}^T \mathbf{D} \mathbf{B}_{NL} \right] d\omega dz \tag{40}$$

$$\mathbf{M} = \int_{-h/2+e}^{h/2-e} \int_{\omega} (1 - \phi)^2 \Phi^T \mathbf{m} \Phi d\omega dz \tag{41}$$

where  $\mathbf{B} = [\mathbf{B}_1, \mathbf{B}_2, \dots, \mathbf{B}_N]$ ,  $\Phi = [\Phi_1, \Phi_2, \dots, \Phi_N]$  and  $\Phi_w = [\Phi_{w1}, \Phi_{w2}, \dots, \Phi_{wN}]$  with  $\Phi_I = \text{diag}[\phi_I, \phi_I, \phi_I, \phi_I, \phi_I]$  and  $\Phi_{wJ} = \text{diag}[0, 0, \phi_J, 0, 0]$ . Meanwhile,  $\hat{\mathbf{D}}_s$  is the modified shear modulus matrix defined by ( $\kappa = 5/6$ )

$$\hat{\mathbf{D}}_s = \frac{\kappa}{1 + \vartheta \cdot (L_e/h)^2} \begin{bmatrix} G_C & 0 \\ 0 & G_C \end{bmatrix} \tag{42}$$

with the largest side length  $L_e$  of the Delaunay triangle. And,  $\vartheta (\vartheta > 0)$  is a shear stabilization parameter, which was determined through a preliminary experiment, as addressed in the next section.

The nonlinear modal Equation (37) was solved using the three-step direct iterative method [48]. At step 1, the linear natural frequencies and natural modes were computed by excluding  $\mathbf{K}_{NL}$  from Equation (37). At step 2, the computed target natural mode  $\bar{\mathbf{d}}$  was scaled up using the desired amplitude–thickness ratio  $w_{max}/h$ , and then, the values of  $\tilde{w}_{,x}$  and  $\tilde{w}_{,y}$  in Equations (18) and (19) were calculated and the nonlinear stiffness matrix  $\mathbf{K}_{NL}$  Was constructed. At step 3, the nonlinear natural frequencies and natural modes were computed. Steps 2 and 3 were repeated until the relative difference between the nonlinear natural frequencies computed at two consecutive iterations was less than 0.1%.

#### 4. Numerical Results

The nonlinear free vibration formulae given in Section 3 for cracked porous cylindrical panels using the phase field theory and the crack rotation concept were coded in the framework of 2-D XNEM [19]. All the stiffness and mass matrices given in Equations (38)–(41) were numerically integrated using 7 Gauss integration points. First, the sensitivity of the present method to the density of 2-D NEM grid was investigated using a clamped intact (i.e., without an internal crack) aluminum cylindrical panel with the geometry dimensions of  $L/R = 2, S/L = 1, R/h = 20$ . In this study, two kinds of boundary conditions, simply supported (S) and clamped (C), were used, and which were implemented as

$$\text{S: } v_0 = \vartheta_y = 0 \tag{43}$$

$$\text{C: } u_0 = v_0 = \omega_0 = \vartheta_x = \vartheta_y = 0 \tag{44}$$

at  $\theta = 0$  or  $\theta_0$ . The component  $v_0$  in Equation (44) was excluded when the clamped condition was specified for the side with  $y = 0$  or  $L$ . The isotropic material properties were  $E_m = 70$  GPa,  $\nu_m = 0.3$  and  $\rho_m = 2707$  kg/m<sup>3</sup>, and the first natural frequency was calibrated as  $\hat{\omega}_1 = \omega_1 L^2 \sqrt{\rho_m / D_m}$  with the flexural rigidity  $D_m = E_m h^3 / 12 (1 - \nu_m^2)$ . The non-dimensional first frequencies  $\hat{\omega}_1$  were computed and are presented in Table 1, where  $\hat{\omega}_1^{rel}$  indicates the relative percentage difference with respect to the fundamental frequency computed with a grid density of  $25 \times 25$ . It was found that the relative difference uniformly decreases in proportion to the grid density such that it becomes less than 3.0% when the grid density goes up to  $21 \times 21$ . So, according to this convergence result, the grid density was set to  $21 \times 21$  for the whole numerical experiment in this paper.

**Table 1.** Dependence of non-dimensional first frequency of an isotropic intact cylindrical panel on the grid density ( $L/R = 2, S/L = 1, R/h = 20, CCCC$ ).

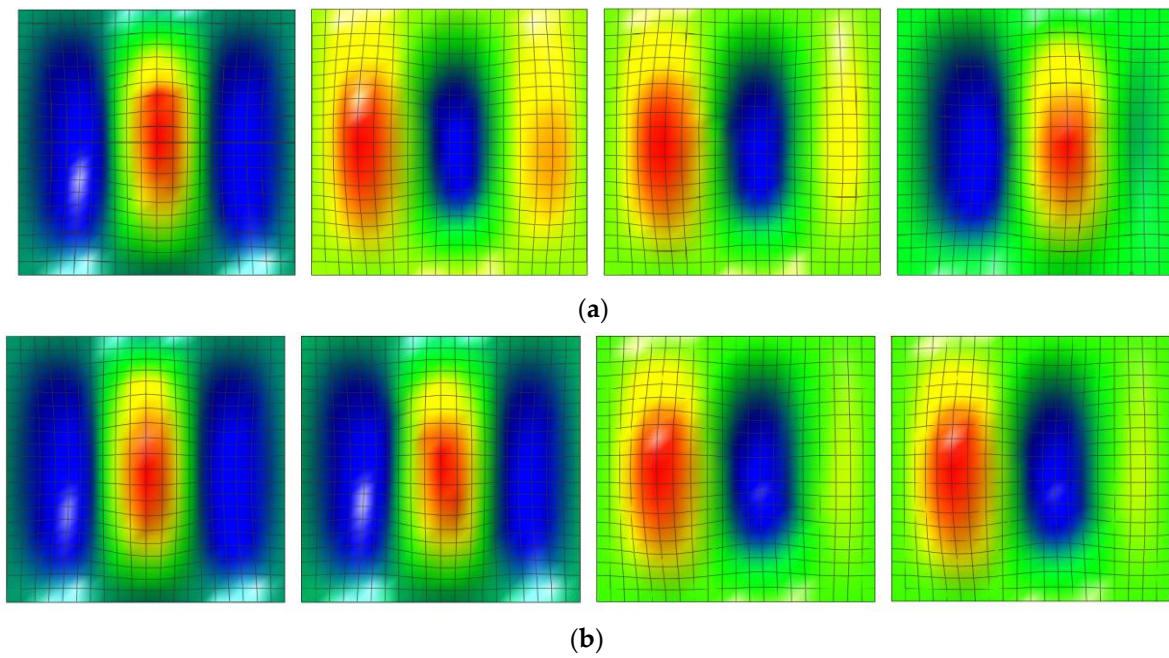
Items	Grid Density						
	13×13	15×15	17×17	19×19	21×21	23×23	25×25
$\hat{\omega}_1$ (Hz)	296.501	288.927	282.838	277.882	273.829	270.491	267.708
$\hat{\omega}_1^{rel}$ (%)	9.70	7.93	5.65	3.80	2.27	1.04	-

Next, the accuracy of the present method was verified by comparing it with the phase field formulation of Torabi and Ansari [36]. A metal–ceramic functionally graded cylindrical panel with an internal crack, shown in Figure 3, is taken. The geometric dimensions and the boundary condition are the same as those from the above convergence test problem, and also, the previous aluminum is taken for the metal while alumina with  $E_c = 380$  GPa and  $\nu_c = 0.26$  is chosen for the ceramic. The power-law function of  $V_c(z) = (0.5 - z/h)^r$  is adopted to identify the thickness-wise volume fractions of the ceramic and also the metal using the relation  $V_m(z) = 1 - V_c(z)$ . The relative crack length  $a/S$  is set at 0.3, while the crack angle and the ceramic power-law index are taken as variables. By comparing with the reference solutions, the shear stabilization factor  $\vartheta$  in Equation (42) was set at  $\vartheta = 0.3 \times [1 - 0.1 \times (1 - \alpha/90)]$  to reflect the influence of crack angle on the stiffness matrix  $K_{L,\sigma}$  in Equation (38). The phase field  $\phi(x)$  in the mass matrix  $M$  in Equation (41) was set to 0 in order to prevent the over-reduction of mass due to an internal crack in the coarse NEM grid. The comparison in Table 2 reveals that the present results show good agreement with the reference solutions, with the maximum relative difference equal to 4.838%. Except for the case of  $\alpha = 0$ , all the present results lead to the relative differences being less than 1.0%. Meanwhile, the fundamental frequency uniformly decreases proportional to the ceramic power-law index  $r$  because the relative region occupied by a stiffer ceramic reduces in proportion to the value of  $r$ . It is found that the first frequency uniformly increases with increasing crack inclination angle because the reduction in the circumferential stiffness of a panel shows that the circumferentially dominated free vibration becomes smaller as the crack inclination angle increases.

**Table 2.** Comparison of first frequencies of ceramic–metal FG cracked cylindrical panels ( $L/R = 2, S/L = 1, R/h = 20, a/S = 0.3, CCCC$ ).

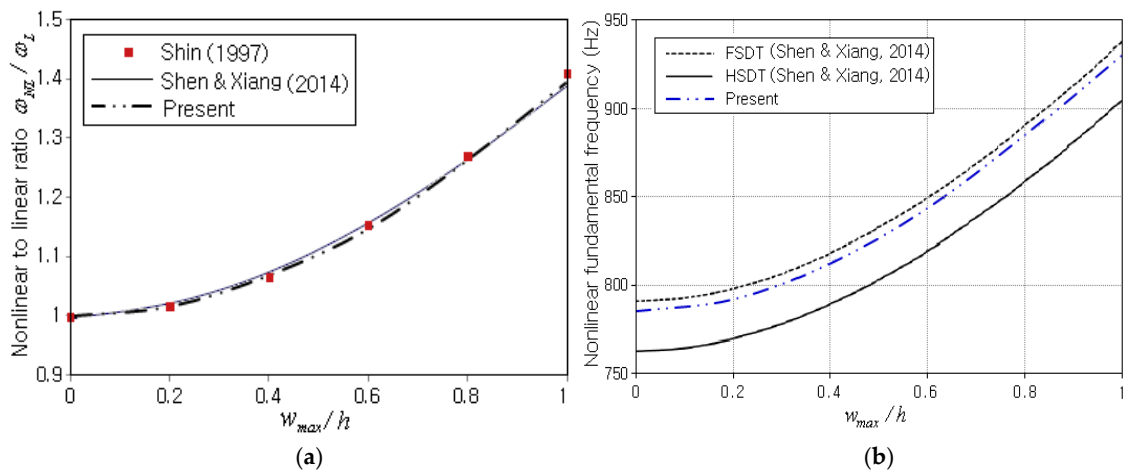
Method	$\alpha$ (deg)	r				
		0	0.2	0.5	1	5
PFF [36]	0	269.69	243.42	215.53	187.67	144.15
	30	274.85	249.43	223.17	196.01	146.73
	60	275.50	250.00	223.67	196.95	147.04
	90	275.73	250.20	223.84	197.09	147.16
Present	0	271.35	247.84	222.83	196.75	145.44
	30	273.25	249.38	223.79	196.96	146.03
	60	275.67	251.18	224.48	196.32	147.09
	90	277.14	251.87	224.69	196.74	148.02

Figure 6a,b comparatively represent the effect of crack inclination angle on the second natural modes for  $a/S = 0.3$  and  $0.6$ , respectively, when the ceramic power-law index  $r$  is 0. The reason for showing the second mode is because the fundamental mode does not produce any apparent change with respect to the crack angle. It is seen that the mode shape becomes separated from the left and right as  $\alpha$  goes to zero, while it becomes similar to the non-separated single plate vibration mode as  $\alpha$  increases.



**Figure 6.** Variation in the second-mode shapes of a clamped FG-GPLRC cylindrical panel to the crack inclination angle ( $\alpha = 0^\circ, 30^\circ, 60^\circ$  and  $90^\circ$ ) for  $r = 0$  (a) at  $a/S = 0.3$  and (b) at  $a/S = 0.6$ .

The present method is also verified through two nonlinear free vibration analyses. One is an isotropic intact cylindrical panel under the simply-supported boundary condition with the geometry and material data given by  $S/L = 1$ ,  $S/h = 10$ ,  $R/h = 0$ ,  $E_m = 68.95$  GPa,  $\nu_m = 0.3$ , and  $\rho_m = 1150$  kg/m<sup>3</sup>. The nonlinear-to-linear frequencies  $\omega_{NL}/\omega_L$  were computed for six different values of amplitude–thickness ratio  $w_{max}/h$ , and the frequency–amplitude plot is compared in Figure 7a. The reference solution by Shin [49] was solved by applying the fourth-order Runge–Kutta method to the FSDT. Meanwhile, the other reference solution by Shen and Xiang [50] was analytically solved by applying a two-step perturbation method to the HSDT. The von Kármán-type geometric nonlinearity was adopted to both solutions, as for the present study. One can clearly see that the three methods are in excellent agreement such that the maximum relative difference in  $\omega_{NL}/\omega_L$  between the present method and that of Shin [49] is 1.149% at  $w_{max}/h = 1.0$ .



**Figure 7.** Comparison of frequency–amplitude curves of isotropic cylindrical panels: (a) non-porous; (b) porous (PD 1) [49,50].

The other nonlinear example is an intact porous isotropic cylindrical panel with the geometric and material data given by  $L = S = 1.0m$ ,  $S/h = 10$ ,  $R/S = 5$ ,  $E_m = 200 \text{ GPa}$ ,  $\nu_m = 0.3$ , and  $\rho_m = 7850 \text{ kg/m}^3$ . The porosity distribution is PD\_1 shown in Figure 2 with the porosity coefficient  $e_0 = 0.6$ , and the four sides of panel are clamped. The computed frequency–amplitude plot is compared with those of Keleshteri and Jelovica [51] in Figure 7b, where two reference solutions were numerically obtained by applying the generalized DQM to FSDT and HSDT. The comparison reveals that the plot of the present method is positioned between HSDT and FSDT, but it is closer to FSDT because the present method is based on FSDT.

Next, the sensitivity of the present phase-field crack model to the grid density was examined using the isotropic cylindrical panel taken from Table 1 in which an inclined central crack is included. The relative length  $a/S$  and the inclination angle  $\alpha$  of a crack were chosen as 0.7 and  $45^\circ$ . The non-dimensional first frequency  $\hat{\omega}_1$  and its linear-nonlinear ratio  $\omega_{NL}/\omega_L$  at  $w_{max}/h = 1.0$  were computed for five grid densities and recorded in Table 3. It is clearly observed that the relative difference of  $\hat{\omega}_1$  uniformly decreases proportional to the grid density. Also, the relative fluctuation in  $\omega_{NL}/\omega_L$  becomes smaller in proportion to the grid density.

**Table 3.** Sensitivity of  $\hat{\omega}_1$  and  $\omega_{NL}/\omega_L$  of a cracked isotropic cylindrical panel to the grid density ( $L/R = 2$ ,  $S/L = 1$ ,  $R/h = 20$ ,  $a/S = 0.7$ ,  $\alpha = 45^\circ$ , CCCC).

Items		Grid Density				
		9×9	13×13	17×17	21×21	25×25
Linear	$\hat{\omega}_1$ (Hz)	37.945	33.505	31.679	31.250	31.191
	$\hat{\omega}_1^{rel}$ (%)	21.65	7.42	1.56	0.19	-
Nonlinear	$\omega_{NL}/\omega_L$ ( $w_{max}/h = 1.0$ )	1.157	1.145	1.166	1.160	1.163
	$(\omega_{NL}/\omega_L)^{rel}$ (%)	-1.81	-1.55	0.26	-0.26	-

The present method was also applied to non-porous FG-GPLRC cylindrical panels with a central crack to examine the influence of crack angle and length, and GPL distribution pattern on the fundamental frequency. The geometric dimensions and the aluminum material properties are the same as those of the first example given in Table 1, where the first frequencies are calibrated as  $\hat{\omega}_1 = \omega_1 S^2 \sqrt{\rho_m/E_m}$ . Meanwhile, the geometric dimensions and the material properties of GPLs are as follows:  $E_{GPL} = 1.01 \text{ TPa}$ ,  $\nu_{GPL} = 0.186$ ,  $l_{GPL} = 2.5 \mu\text{m}$ ,  $w_{GPL} = t_{GPL} = 1.5 \mu\text{m}$ , and  $\rho_{GPL} = 10600 \text{ kg/m}^3$ , respectively. It is observed from Table 4 that the non-dimensional fundamental frequency decreases proportionally to the crack length because the panel stiffness decreases as the crack length increases. Meanwhile, regarding the GPL distribution pattern, FG-X leads to the highest level while FG-O shows the lowest level. This relative order among the GPL distribution patterns is attributed to the fact that the panel stiffness becomes higher as GPLs become biased towards the top and bottom of the panel; see Figure 1b.

Next, the nonlinear natural vibration of the clamped FG-GPLRC cylindrical panel with a central crack was profoundly examined by changing the major parameters. Figure 8a represents the effect of crack inclination angle on the variation in nonlinear-to-linear frequency ratio  $\omega_{NL}/\omega_L$  to the amplitude–thickness ratio  $w_c^{max}/h$ . The mass fraction  $g_{GPL}^*$  and distribution pattern of GPLs are 0.4% and FG-U, and the relative crack length  $a/S$  is set at 0.3. It is seen that the frequency ratio  $\omega_{NL}/\omega_L$  becomes uniformly smaller in proportion to the crack inclination angle, but the decrease trend becomes smaller proportional to the crack angle. Thus, this trend reveals that the nonlinearity in free vibration decreases with increasing crack inclination angle. Figure 8b represents the effect of crack relative length on the nonlinear natural vibration of the FG-U GPLRC cylindrical panel when the crack inclination angle  $\alpha$  is zero. It is seen that the frequency ratio  $\omega_{NL}/\omega_L$  becomes slightly smaller with increasing crack relative length because the panel stiffness drops proportional to the crack relative length.

**Table 4.** Non-dimensional first frequencies  $\hat{\omega}_1$  of non-porous FG-GPLRC cylindrical panels with a central crack ( $L/R = 2, S/L = 1, R/h = 20, g_{GPL}^* = 0.4\%, CCCC$ ).

Crack Length $a/S$	Crack Angle $\alpha(deg)$	GPL Distribution			
		FG-U	FG-O	FG-X	FG- $\Lambda$
0.3	0	50.0201	45.2187	51.9930	48.3275
	30	50.1616	45.8623	52.2722	48.9641
	60	50.2431	46.8017	52.3461	49.4227
	90	50.3914	46.8707	52.4892	49.5481
0.6	0	47.8834	44.4466	49.7297	47.1588
	30	48.2756	44.8122	50.2369	47.7287
	60	48.3421	45.0171	50.4532	47.8063
	90	49.0014	45.8415	50.9793	48.2326

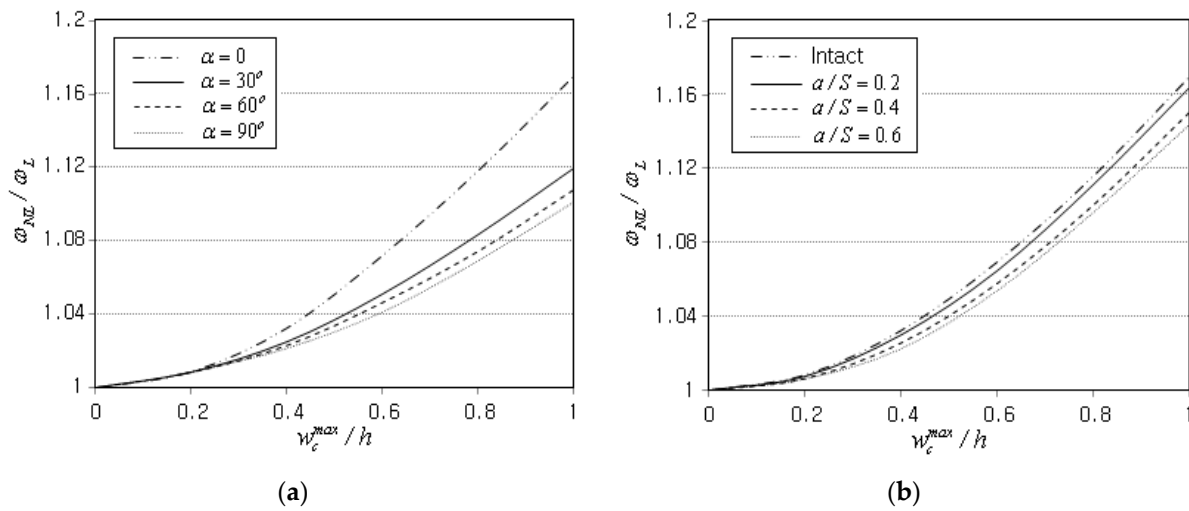


**Figure 8.** Variation in nonlinear-to-linear frequency ratio  $\omega_{NL}/\omega_L$  (FG-U,  $g_{GPL}^* = 0.4\%, a/S = 0.3$ ) (a) to the crack angle  $\alpha$  and (b) to the crack relative length  $a/S$  ( $\alpha = 0^\circ$ ).

Figure 9a represents the variation in frequency ratio  $\omega_{NL}/\omega_L$  to the GPL mass fraction  $g_{GPL}^*$  for the FG-O GPLRC cylindrical panel with a central crack. The inclination angle and relative length of a crack are set at  $30^\circ$  and 0.3. Each nonlinear free vibration analysis for five values of  $w_c^{max}/h$  was completed within five minutes on an Intel Pentium PC with a dual core CPU (1.86 GHz). It is observed that the frequency ratio uniformly increases in proportion to the GPL mass fraction because the mass fraction increase in GPLs with a higher elastic modulus leads to an increase in panel stiffness. Figure 9b represents the influence of the GPL distribution pattern on the frequency ratio  $\omega_{NL}/\omega_L$ , for which the GPL mass  $g_{GPL}^*$  was set to 0.4%, while three different GPL distribution patterns were additionally considered. It is found that the magnitude order of frequency ratio  $\omega_{NL}/\omega_L$  is FG-X, FG-O, FG-U, and FG- $\Lambda$ . This trend is slightly different from the magnitude order of linear fundamental frequency  $\hat{\omega}_1$  given in Table 3, where FG-O shows the lowest level. In the frequency ratio  $\omega_{NL}/\omega_L$ , FG-O shows the second highest level, which is caused by the fact that the magnitude of  $\omega_{NL}/\omega_L$  is not determined by the magnitudes of  $\omega_{NL}$  and  $\omega_L$  but the relative value of these two. This trend was also observed from Figure 8a, where larger inclination crack angles showed lower frequency ratios  $\omega_{NL}/\omega_L$  even though the linear fundamental frequency was higher at larger inclination crack angles.

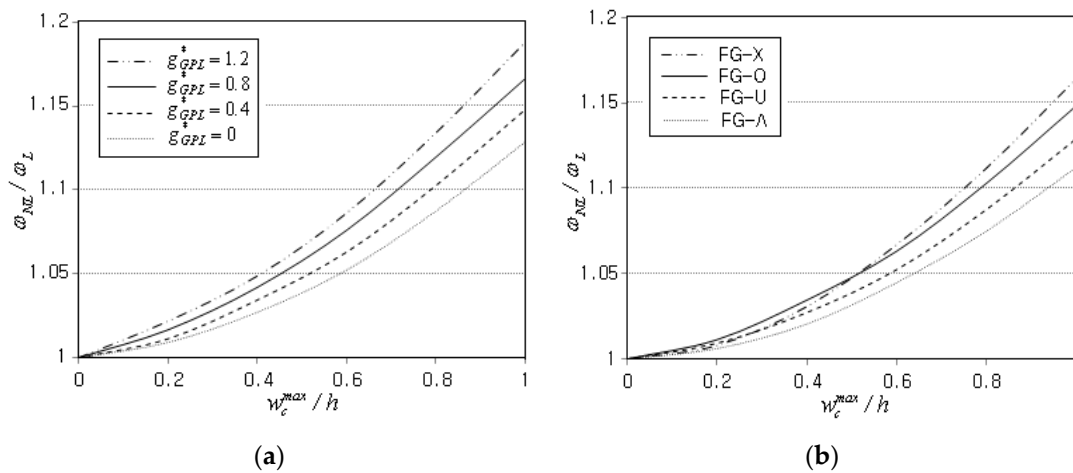


**Figure 9.** Variation in nonlinear-to-linear frequency ratio  $\omega_{NL}/\omega_L$  ( $a/S = 0.3, \alpha = 30^\circ$ ) (a) to the GPL mass fraction  $\xi_{GPL}^*$  (FG-O) and (b) to the GPL distribution pattern ( $\xi_{GPL}^* = 0.4\%$ ).

Next, the nonlinear free vibration of the cracked cylindrical panel between GPLRC and CNTRC was compared by keeping the material properties of the matrix unchanged. The (10,10) single-walled CNTs [52] were taken, and their orthotropic material properties are presented in Table 5. The effective material properties of the CNTRC structures are evaluated as

$$E_1 = \eta_1 f_{CNT} E_1^{CNT} + f_m E_m, \quad \frac{\eta_2}{E_2} = \frac{f_{CNT}}{E_2^{CNT}} + \frac{f_m}{E_m} \tag{45}$$

$$\frac{\eta_3}{G_{12}} = \frac{f_{CNT}}{G_{12}^{CNT}} + \frac{f_m}{G_m}, \quad \nu_{12} = f_{CNT} \nu_{12}^{CNT} + f_m \nu_m \tag{46}$$

according to the modified linear rule of mixtures (MLRMs), where the CNT efficiency parameters  $\eta_i$  ( $i = 1, 2, 3$ ) are dependent of the CNT total volume fraction  $V_{CNT}^*$  [53]. Note that LRM accounts only for matrix-fiber deformation but does not consider nonlinearities such as fiber–matrix adhesion that might consume a large chunk of applied energy.

**Table 5.** Material properties of (10,10) single-walled CNTs ( $1, 2, 3 = x, y, z$ ).

Elastic Moduli (GPa)			Poisson’s Ratios			Shear Moduli (GPa)		
$E_1^{cnt}$	$E_2^{cnt}$	$E_3^{cnt}$	$\nu_{12}^{cntT}$	$\nu_{23}^{cnt}$	$\nu_{31}^{cnt}$	$G_{12}^{cnt}$	$G_{23}^{cnt}$	$G_{31}^{cnt}$
5646.6	7080.0	-	0.175	-	-	1944.5	-	-

Figure 10a represents the variation in  $\omega_{NL}/\omega_L$  to the relative central amplitude  $w_c^{max}/h$  of a cracked FG-X cylindrical panel with  $a/S = 0.3$  and  $\alpha = 30^\circ$ , where the angle  $\alpha_{CNT} = 90^\circ$  denotes that CNTs are aligned in the direction of cylinder axis. The frequency ratio  $\omega_{NL}/\omega_L$  shows a noticeable change to the CNT volume fraction  $V_{CNT}^*$ , even though the extent of increase is not so large when compared with that shown in Figure 9a. Figure 10b represents the variation for different GPL volume fractions  $V_{GPL}^*$ , where the ratio  $\omega_{NL}/\omega_L$  and its dependence on  $V_{GPL}^*$  are shown to be smaller than those shown in Figure 10a. Note, from the relation in Equation (3), that  $V_{GPL}^* = 0.12$  equals 10.75% of the GPL mass fraction. Therefore, it is found that the dependence of frequency ratio  $\omega_{NL}/\omega_L$  on  $V_{GPL}^*$  and  $V_{CNT}^*$  becomes insensitive in proportion to the amount of GPLs and CNTs, and this trend is more apparent at CNTRC for the same volume fraction. This is because the nonlinearity intensity becomes saturated as the structural stiffness reaches the critical value owing to the increase in CNTs and GPLs, as will be seen later.

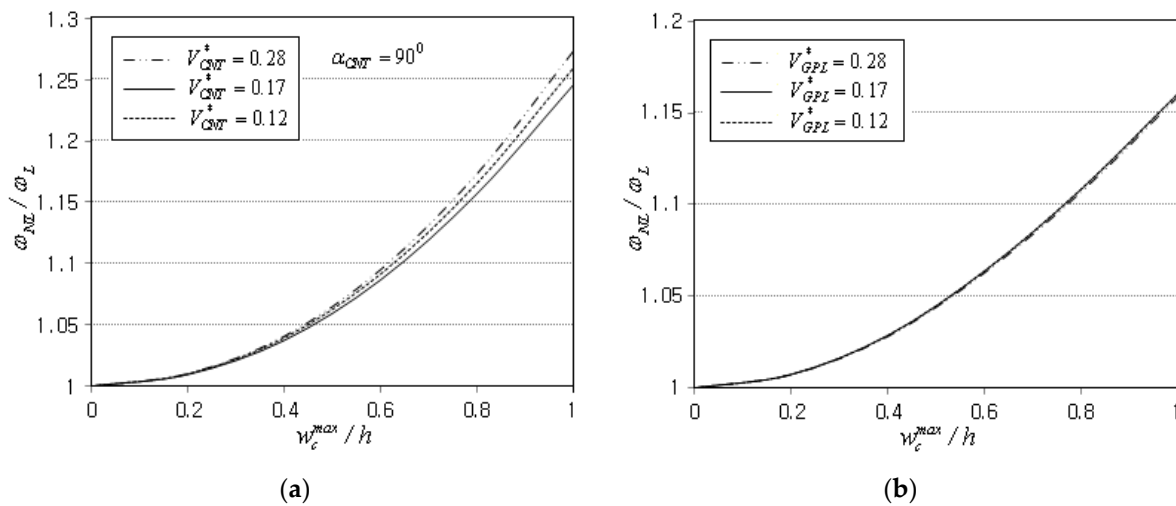


**Figure 10.** Comparison of nonlinear-to-linear frequency ratios  $\omega_{NL}/\omega_L$  between GPLRC and CNTRC (FG-X,  $a/S = 0.3$ ,  $\alpha = 30^\circ$ ): (a) CNTRC; (b) GPLRC.

Before the examination of the effect of higher  $V_{GPL}^*$  and  $V_{CNT}^*$  on the variation in  $\omega_{NL}/\omega_L$ , the fundamental frequencies of GPLRC and CNTRC are compared for the FG-X cylindrical panel with  $a/S = 0.3$  and  $\alpha = 30^\circ$ . From Table 6, it is found that the first frequencies of GPLRC are much higher than those of CNTRC, implying that GPLRC possesses much higher structural stiffness than CNTRC for the same volume fraction. This is because the material properties of CNTRC are axis-dependent such that the two lateral elastic moduli are much lower than the axial one. It is clearly found that the non-dimensional first frequency of CNTRC becomes higher when the CNTs are aligned in the circumferential direction (i.e.,  $\alpha_{CNT} = 0^\circ$ ).

**Table 6.** The non-dimensional linear first frequencies  $\hat{\omega}_1$  (FG-X,  $a/S = 0.3$ ,  $\alpha = 30^\circ$ ).

Type		Volume Fraction $V_{GPL}^* = V_{CNT}^* (g_{GPL}^*)$		
		0.12 (10.75%)	0.17 (15.32%)	0.28 (25.57%)
GPLRC		216.31	258.31	335.64
CNTRC	$\alpha_{CNT} = 90^\circ$	39.19	50.64	55.55
	$\alpha_{CNT} = 0^\circ$	56.03	72.20	80.32

Figure 11a represents the variation in  $\omega_{NL}/\omega_L$  with respect to the GPL mass fraction  $g_{GPL}^*$  for different GPL distribution patterns when  $\omega_c^{max}/h$  is 1.0. It is seen that the frequency ratio  $\omega_{NL}/\omega_L$  becomes saturated such that FG-O and FG- $\Lambda$  approach the upper bounded value while FG-U and FG-X approach the lower bounded value. Thus, it has been justified that the nonlinearity intensity in the free vibration becomes insensitive to  $V_{GPL}^*$  and  $V_{CNT}^*$  when the amount of GPLs and CNTs reaches a critical value. Figure 11b represents the variation in  $\omega_{NL}/\omega_L$  to the CNT volume fraction when CNTs are aligned in the circumferential direction. The relative order in the magnitude of  $\omega_{NL}/\omega_L$  is the same as that of  $\alpha_{CNT} = 90^\circ$ , shown in Figure 10a, but the magnitude of  $\omega_{NL}/\omega_L$  and its sensitivity to  $V_{CNT}^*$  are shown to be relatively larger than those of CNTRC with  $\alpha_{CNT} = 90^\circ$ . It is noticed that the  $\omega_{NL}/\omega_L$  of  $V_{CNT}^* = 0.17$  is smaller than the  $\omega_{NL}/\omega_L$  of  $V_{CNT}^* = 0.12$  regardless of the CNT alignment angle. It is of course attributed to the fact that both the  $\omega_L$  and  $\omega_{NL}$  of  $V_{CNT}^* = 0.17$  are larger those of  $V_{CNT}^* = 0.12$  but their relative ratio can be smaller than that of  $V_{CNT}^* = 0.12$ .

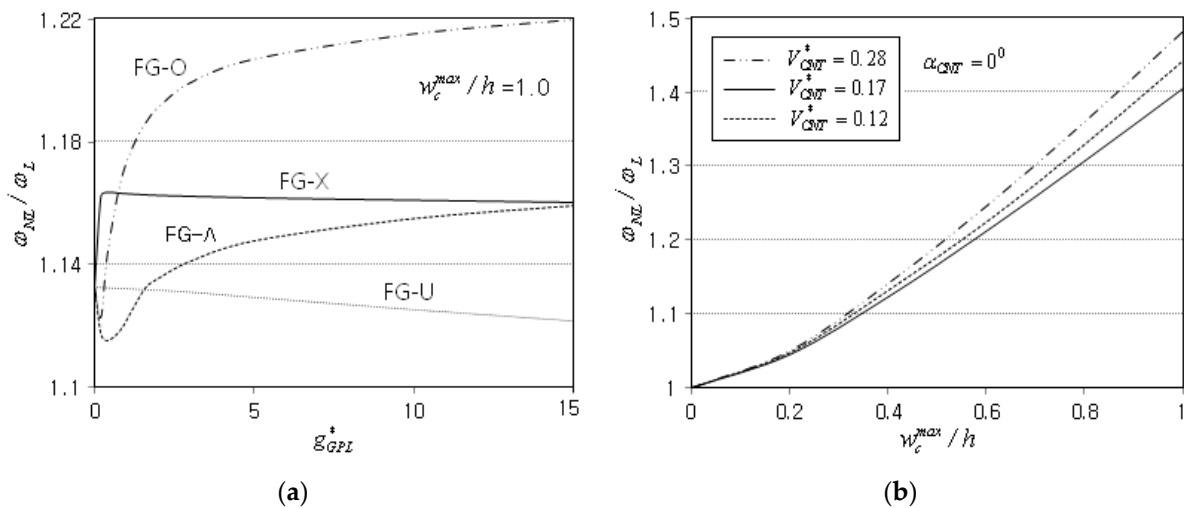
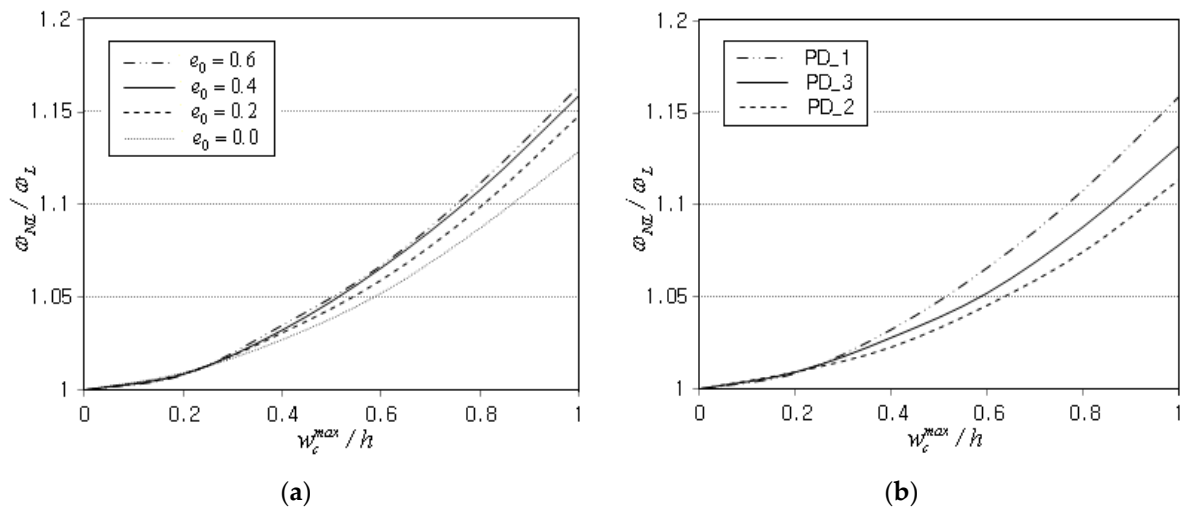


**Figure 11.** Nonlinear-to-linear frequency ratio  $\omega_{NL}/\omega_L$ : (a) dependence on  $g_{GPL}^*$  for  $w_c^{max}/h = 1$  and (b) for CNTRC with  $\alpha_{CNT} = 0^\circ$ .

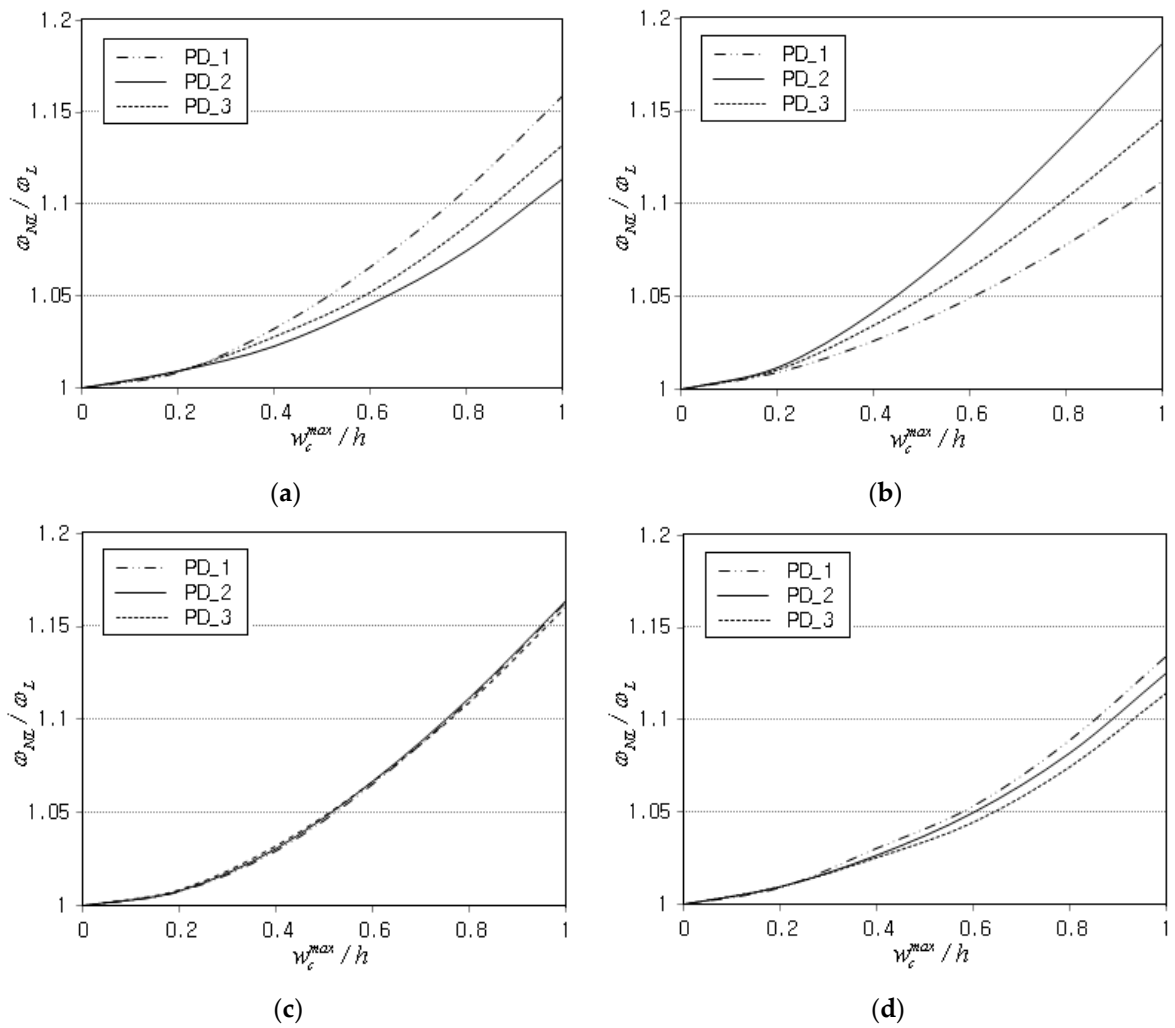
Next, the influence of porosity on the nonlinear free vibration of a cracked FG-GPLRC cylindrical panel was investigated. The mass fraction  $g_{GPL}^*$  and distribution pattern are 0.4% and FG-U, and the inclination angle  $\alpha$  and relative length  $a/S$  of the crack are  $30^\circ$ . Three different porosity distributions and the five porosity parameters were considered.

Figure 12a comparatively represents the frequency ratios  $\omega_{NL}/\omega_L$  of an FG-U GPLRC cylindrical panel with the center-biased porosity distribution (PD\_1). It is observed that the frequency ratio becomes uniformly smaller with the increase in  $e_0$  until  $w_c^{max}/h = 0.2$ , but thereafter, it uniformly increases in proportion to  $e_0$ . However, the extent of decrease becomes smaller as the porosity parameter  $e_0$  increases. Both  $\omega_L$  and  $\omega_{NL}$  decrease proportionally to  $e_0$  because the increase in porosity decreases the structural stiffness [54]. But, the frequency ratio  $\omega_{NL}/\omega_L$  may increase with increasing  $e_0$  because the denominator  $\omega_L$  decreases in proportion to  $e_0$ . Figure 12b compares the plots of  $\omega_{NL}/\omega_L$  for three different porosity distributions, where the center-biased distribution (PD\_1) shows the highest level while the outer-biased distribution (PD\_2) leads to the lowest level. This is because the structural stiffness increases as the porosity becomes biased towards the mid-surface of panel for the same amount of porosity. However, the relative difference in  $\omega_{NL}/\omega_L$  among the three porosity distributions becomes different when the GPL distribution pattern is changed, as will be seen next.

Figure 13a–d comparatively represent the differences in  $\omega_{NL}/\omega_L$  between three porosity distributions for FG-U, G-O, FG-X, and FG- $\wedge$ . First of all, it is clearly observed that the relative order and difference in the three plots of  $\omega_{NL}/\omega_L$  are remarkably influenced by the GPL distribution pattern. In FG-O, shown in Figure 13b, the center-biased PD\_1 shows the lowest level because the middle region with a high density of GPLs is mostly occupied with pores. On the other hand, the outer-biased PD\_2 shows the highest level because most pores are concentrated in the top and bottom regions with a low density of GPLs. In FG-X, shown in Figure 13c, the difference between three porosity distributions is negligible. It is because the relative increase in  $\omega_{NL}$  with respect to  $\omega_L$  is almost similar for the three porosity distributions as the amplitude–thickness ratio  $w_c^{max}/h$  increases. Meanwhile, in FG- $\wedge$ , shown in Figure 13d, the three porosity distributions show noticeable difference because the GPLs are concentrated only in the bottom region, differing from FG-X. Thus, it is found that the combination of GPL and porosity distributions leads to more diverse variations in the nonlinear-to-linear frequency ratio.



**Figure 12.** Variation in nonlinear-to-linear frequency ratio  $\omega_{NL}/\omega_L$  (FG-U,  $g_{GPL}^* = 0.4\%$ ,  $a/S = 0.3$ ,  $\alpha = 30^\circ$ ) (a) to the porosity parameter  $e_0$  (PD-1) and (b) to the porosity distribution pattern ( $e_0 = 0.3$ ).



**Figure 13.** Comparison of nonlinear-to-linear frequency ratios  $\omega_{NL}/\omega_L$  ( $g_{GPL}^* = 0.4\%$ ,  $e_0 = 0.4$ ,  $a/S = 0.3$ ,  $\alpha = 30^\circ$ ) (a) for FG-U, (b) for FG-O, (c) for FG-X, and (d) for FG- $\Delta$ .

### 5. Conclusions

The nonlinear free vibration of a porous FG-GPLRC cylindrical panel with a central crack has been investigated by combining a phase field formulation and a virtual geometry rotation in the framework of 2-D XNEM. The curved neutral surface was transformed into a rectangular plane for the easy definition and manipulation of L/I functions, and the troublesome numerical locking was effectively suppressed by employing the MITC3+ shell concept and the stabilization factor. The developed nonlinear numerical method was verified through a comparison with the reference solutions, and the nonlinear free vibration characteristics of cracked porous FG-GPLRC cylindrical panels were profoundly examined. The numerical results led to the following major findings:

- The present method shows stable convergence and good agreement with the reference solutions, with a maximum relative difference equal to 4.838%.
- The nonlinear-to-linear frequency ratio  $\omega_{NL}/\omega_L$  decreases with increasing crack inclination angle, but the decreasing slope becomes saturated. Meanwhile, it uniformly decreases as the relative crack length becomes larger.
- The frequency ratio  $\omega_{NL}/\omega_L$  increases in proportion to the GPL mass fraction  $g_{GPL}^*$ , but it becomes saturated as  $g_{GPL}^*$  increases over a critical value. And, the saturation trend is different for different GPL distribution patterns.
- The frequency ratio  $\omega_{NL}/\omega_L$  increases proportionally to the porosity coefficient  $e_0$  even though it shows a saturation trend. Also, its variation to  $w_c^{max}/h$  is remarkably affected by the porosity distribution and becomes more diverse when the GPL distribution is combined.
- Compared with FG-GPLRC, FG-CNTRC produces a remarkably lower linear fundamental frequency but a slightly higher frequency ratio  $\omega_{NL}/\omega_L$ , for the same volume fraction. In addition, its nonlinear free vibration is affected by the CNT alignment direction, differing from FG-CNTRC.

**Funding:** This work was supported by the 2024 Hongik University Research Fund.

**Data Availability Statement:** The original contributions presented in the study are included in the article, further inquiries can be directed to the corresponding author.

**Conflicts of Interest:** The author declares no conflict of interest.

### Appendix A. Interpolation of T/S Strains

The geometry transformation  $T_C$  from the computational NEM grid  $\mathfrak{S}_R = [0, \theta_0] \times [0, L]$  to the physical NEM grid  $\mathfrak{S}_C = [0, S] \times [0, L]$  is defined by

$$T_C : (\zeta_1, \zeta_2) \in \mathfrak{S}_R \rightarrow (x, y) \in \mathfrak{S}_C \tag{A1}$$

Then, the L/I functions  $\psi_J(x, y)$  are mapped to  $\phi_J(\zeta_1, \zeta_2)$ , and the two relations  $x = R \cdot \zeta_1$  and  $y = \zeta_2$  lead to the inverse Jacobi matrix  $J^{-1}$  given by

$$J^{-1} = \begin{bmatrix} \partial\zeta_1/\partial x & \partial\zeta_1/\partial y \\ \partial\zeta_2/\partial x & \partial\zeta_2/\partial y \end{bmatrix} = \begin{bmatrix} 1/R & 0 \\ 0 & 1 \end{bmatrix} \tag{A2}$$

As well, the partial derivatives  $L_x$  and  $L_y$  in Equations (18)–(20) defined on the panel neutral surface are changed to

$$\frac{\partial}{\partial x} = L_x = \frac{1}{R} \frac{\partial}{\partial \zeta_1} = \frac{1}{R} L_1, \quad \frac{\partial}{\partial y} = L_y = \frac{\partial}{\partial \zeta_2} = L_2 \tag{A3}$$

defined on the 2-D rectangular NEM grid according to the chain rule.

Introducing Equation (A3) into Equations (20)–(22) leads to  $\hat{L}$  and  $\hat{L}_s$  in which  $L_x$  and  $L_y$  are replaced with  $L_1$  and  $L_2$ :

$$T_C^{-1} : L, L_s \rightarrow \tilde{L}, \tilde{L}_s \tag{A4}$$

### Appendix B. Interpolation of T/S Strains

Each triangle  $\omega_e$  in the physical NEM grid  $\mathfrak{S}_C$  shown in Figure 4 is mapped to the three-node master element  $\hat{\omega}$  in Figure A1. And, the non-singular displacement part is re-expressed using the computed triangle-wise nodal vectors  $b_K^e = (u_0^e, v_0^e, w_0^e, \beta_x^e, \beta_y^e)^T_K$  and the Lagrange-type bilinear shape functions  $\{N_L(\xi, \eta)\}_{L=1}^3$ . Next, according to the MITC3+ shell approach, the triangle-wise T/S strains  $\gamma_e^h$  are indirectly interpolated as

$$(\gamma_e^h)_{xz} = \frac{2}{3} \left[ \gamma_{xz}^{(B)} - \frac{1}{2} \gamma_{yz}^{(B)} \right] + \frac{1}{2} \left[ \gamma_{xz}^{(C)} + \gamma_{yz}^{(C)} \right] + \frac{\delta}{3} (3\eta - 1) \tag{A5}$$

$$(\gamma_e^h)_{yz} = \frac{2}{3} \left[ \gamma_{yz}^{(A)} - \frac{1}{2} \gamma_{xz}^{(A)} \right] + \frac{1}{2} \left[ \gamma_{yz}^{(C)} + \gamma_{xz}^{(C)} \right] + \frac{\delta}{3} (1 - 3\xi) \tag{A6}$$

with  $\delta = \gamma_{xz}^{(F)} - \gamma_{xz}^{(D)} + \gamma_{yz}^{(E)} - \gamma_{yz}^{(B)}$ , where A, B, C, D, E, and F indicate the six tying points, as shown in Figure A1.

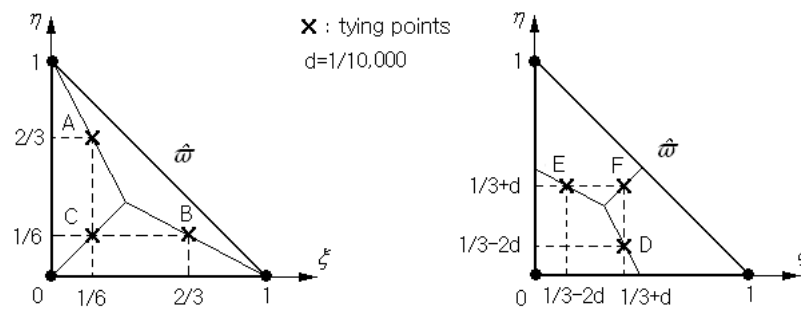


Figure A1. Locations of the six tying points within the master triangular element  $\hat{\omega}$ .

### References

- Shi, G.; Araby, S.; Gibson, C.T.; Meng, Q.; Zhu, S.; Ma, J. Graphene platelets and their polymer composites: Fabrication, structure, properties, and applications. *Adv. Funct. Mater.* **2018**, *28*, 1706705. [CrossRef]
- Soni, S.K.; Thomas, B.; Kar, V.R. A comprehensive review on CNTs and CNT-reinforced composites: Syntheses, characteristics and applications. *Mater. Today Commun.* **2020**, *25*, 101546. [CrossRef]
- Cho, J.R.; Ahn, Y.J. Investigation of mechanical behaviors of functionally graded CNT-reinforced composite plates. *Polymers* **2022**, *14*, 2664. [CrossRef] [PubMed]
- King, J.A.; Klimek, D.R.; Miskioglu, I.; Odegard, G.M. Mechanical properties of graphene nanoplatelet/epoxy composites. *J. Compos. Mater.* **2014**, *49*, 659–669. [CrossRef]
- Zegeye, E.; Ghamsari, A.K. Mechanical properties of grapheme platelets reinforced syntactic foams. *Compos. Part B* **2014**, *60*, 268–273. [CrossRef]
- Liew, K.M.; Jianwei, Y.; Zhang, L.W. *Mechanical Behaviors of Carbon Nanotubes: Theoretical and Numerical Approaches*; Elsevier: Amsterdam, The Netherlands, 2016.
- Cho, J.R.; Oden, J.T. Functionally graded material: A parametric study on thermal-stress characteristics using the Crack-Nicolson-Galerkin scheme. *Comput. Methods Appl. Mech. Eng.* **2000**, *188*, 17–38. [CrossRef]
- Suresh, S.; Giannakopoulos, A.E.; Olson, M. Elastoplastic analysis of thermal cycling: Layered materials with sharp interfaces. *J. Mech. Phys. Solids* **1994**, *42*, 978–1018. [CrossRef]
- Zhao, S.; Zhao, Z.; Yang, Z.; Ke, L.L.; Yang, J.; Kitipornchai, S. Functionally graded graphene reinforced composite structures: A review. *Eng. Struct.* **2020**, *210*, 110339. [CrossRef]
- Liew, K.M.; Pan, Z.; Zhang, L.W. The recent progress of functionally graded CNT reinforced composites and structures. *Sci. China Phys. Mech. Astron.* **2019**, *63*, 234601. [CrossRef]
- Zhu, J.C.; Lai, Z.H.; Jeon, J.; Lee, S. Fabrication of ZrO<sub>2</sub>-NiCr functionally graded material by powder metallurgy. *Mater. Chem. Phys.* **2001**, *68*, 130135. [CrossRef]

12. Kieback, B.; Neubrand, A.; Riedel, H. Processing techniques for functionally graded materials. *Mater. Sci. Eng. A* **2003**, *362*, 81–105. [[CrossRef](#)]
13. Setoodeh, A.R.; Shojaee, M.; Malekzadeh, P. Vibrational behavior of doubly curved smart sandwich shells with FG-CNTRC face sheets and FG porous core. *Compos. Part B Eng.* **2019**, *165*, 798–822. [[CrossRef](#)]
14. Yang, Z.; Wu, D.; Yang, J.; Lai, S.K.; Lv, J.; Fiu, J. Dynamic buckling of rotationally restrained FG porous arches reinforced with graphene nanoplatelets under a uniform step load. *Thin-Walled Struct.* **2021**, *166*, 108103. [[CrossRef](#)]
15. Cho, J.R. Free vibration analysis of functionally graded porous cylindrical panels reinforced with graphene platelets. *Nanomaterials* **2023**, *13*, 1441. [[CrossRef](#)] [[PubMed](#)]
16. Wu, H.; Yang, J.; Kitipornchai, S. Mechanical analysis of functionally graded porous structures: A review. *Int. J. Struct. Stab. Dyn.* **2020**, *20*, 2041015. [[CrossRef](#)]
17. Young, R.J.; Kinloch, I.A.; Gong, I.; Novoselov, K.S. The mechanics of graphene nano composites: A review. *Compos. Sci. Technology* **2012**, *72*, 1459–1476. [[CrossRef](#)]
18. Rafiee, M.A.; Rafiee, J.; Wang, Z.; Song, H.; Yu, Z.Z.; Koratkar, N. Enhanced mechanical properties of nanocomposites at low graphene content. *ACS Nano* **2009**, *3*, 3884–3890. [[CrossRef](#)] [[PubMed](#)]
19. Cho, J.R. Investigation of buckling behavior of cracked FG cylindrical panels reinforced by graphene platelets. *Symmetry* **2023**, *15*, 2162. [[CrossRef](#)]
20. Halpin, J.C.; Kardos, J.L. The Halpin-Tsai equations: A review. *Polym. Eng. Sci.* **1976**, *16*, 344–352.
21. Feng, C.; Kitipornchai, S.; Yang, J. Nonlinear free vibration of functionally graded polymer composite beams reinforced with graphene nanoplatelets (GPLs). *Eng. Struct.* **2017**, *140*, 110–119. [[CrossRef](#)]
22. Zhang, L.W.; Zhang, Y.; Liew, K.M. Modeling of nonlinear vibration of graphene sheets using a meshfree method based on nonlocal elasticity theory. *Appl. Math. Model.* **2017**, *49*, 691–704. [[CrossRef](#)]
23. Gao, K.; Gao, W.; Chen, D.; Yang, J. Nonlinear free vibration of functionally graded graphene platelets reinforced porous nanocomposite plates resting on elastic foundations. *Compos. Struct.* **2018**, *204*, 831–846. [[CrossRef](#)]
24. Shen, H.S.; Xiang, Y.; Fan, Y.; Hui, D. Nonlinear vibration of functionally graded graphene-reinforced composite laminated cylindrical panels resting on elastic foundations in thermal environments. *Compos. Part B Eng.* **2018**, *136*, 177–186. [[CrossRef](#)]
25. Kiani, Y. Isogeometric large amplitude free vibration of graphene reinforced laminated plates in thermal environment using NURBS formulation. *Comput. Methods Appl. Mech. Eng.* **2018**, *332*, 86–101. [[CrossRef](#)]
26. Teng, M.W.; Wang, Y.Q. Nonlinear free vibration of rectangular plates reinforced with 3D graphene form: Approximate analytical solution. *Results Phys.* **2020**, *17*, 103147. [[CrossRef](#)]
27. Song, M.; Gong, Y.; Yang, J.; Zhu, W.; Kitipornchai, S. Nonlinear free vibration of cracked functionally graded graphene platelet-reinforced nanocomposite beams in thermal environments. *J. Sound Vib.* **2020**, *468*, 115115. [[CrossRef](#)]
28. Tao, C.; Dai, T. Isogeometric analysis for size-dependent nonlinear free vibration of graphene platelet reinforced laminated annular sector microplates. *Eur. J. Mech.-A/Solids* **2021**, *86*, 104171. [[CrossRef](#)]
29. Javani, M.; Kiani, Y.; Eslami, M.R. Geometrically nonlinear free vibration of FG-GPLRC circular plate on nonlinear elastic foundation. *Compos. Struct.* **2021**, *261*, 113515. [[CrossRef](#)]
30. Wang, Y.; Chen, J. Nonlinear free vibration of rotating functionally graded graphene platelets reinforced blades with variable cross-sections. *Eng. Anal. Bound. Elem.* **2022**, *144*, 262–278. [[CrossRef](#)]
31. Wang, K.; Chen, L.; Wu, J.; Toh, M.L.; He, C.; Yee, A.F. Epoxy nanocomposites with highly exfoliated clay: Mechanical properties and fracture mechanisms. *Macromolecules* **2005**, *38*, 788–800. [[CrossRef](#)]
32. Moes, N.; Dolbow, J.; Belytschko, T. A finite element method for crack growth without remeshing. *Int. J. Numer. Methods Eng.* **1999**, *46*, 131–150. [[CrossRef](#)]
33. Cho, J.R. Near-tip grid refinement for the effective and reliable natural element crack analysis. *Struct. Eng. Mech.* **2019**, *70*, 279–287. [[CrossRef](#)]
34. Wang, C.; Wang, Y.; Cui, B.; Duan, L.; Ma, N.X.; Feng, J.Q. Numerical simulation of distortion-induced fatigue crack growth using extended finite element method. *Struct. Infrastruct. Eng.* **2020**, *16*, 106–122. [[CrossRef](#)]
35. Ambati, M.; Gerasimov, T.; De Lorenzis, L. A review on phase-field models of brittle fracture and a new fast hybrid formulation. *Comput. Mech.* **2015**, *55*, 383–405. [[CrossRef](#)]
36. Torabi, J.; Ansari, R. Numerical investigation on the buckling and vibration of cracked FG cylindrical panels based on the phase-field formulation. *Eng. Fract. Mech.* **2020**, *228*, 106895. [[CrossRef](#)]
37. Mohammadi, S. *Extended Finite Element Method: For Fracture Analysis of Structures*; John Wiley & Sons: Hoboken, NJ, USA, 2008.
38. Bayesteh, H.; Mohammadi, S. XFEM fracture analysis of shells: The effect of crack tip enrichments. *Comput. Mater. Sci.* **2011**, *50*, 793–813. [[CrossRef](#)]
39. Cho, J.R.; Oden, J.T. Locking and boundary layer in hierarchical models for thin elastic structures. *Comput. Methods Appl. Mech. Eng.* **1997**, *149*, 33–48. [[CrossRef](#)]
40. Pitkaranta, J. The problem of membrane locking in finite element analysis of cylindrical shells. *Numer. Isch. Mathematik* **1992**, *61*, 523–542. [[CrossRef](#)]
41. Lee, Y.; Lee, P.S.; Bathe, K.J. The MITC3+shell finite element and its performance. *Comput. Struct.* **2014**, *138*, 12–23. [[CrossRef](#)]
42. Cho, J.R. Neutral surface-based static and free vibration analysis of functionally graded porous plates. *Steel Compos. Struct.* **2023**, *49*, 431–440.

43. Gibson, L.J.; Ashby, M.F. The mechanics of three-dimensional cellular materials. *Proc. R. Soc. Lond. A Math. Phys. Eng. Sci. R. Soc.* **1982**, *382*, 43–59.
44. de Borst, R.; Verhoosel, C.V. Gradient damage vs phase-field approaches for fracture: Similarities and differences. *Comput. Methods Appl. Mech. Eng.* **2016**, *312*, 78–94. [[CrossRef](#)]
45. Hirshikesh; Natarajan, S.; Annabattula, R.K.; Martinez-Paneda, E. Phase field modeling of crack propagation in functionally graded materials. *Compos. Part B Eng.* **2019**, *169*, 239–248. [[CrossRef](#)]
46. Cho, J.R.; Lee, H.W. A Petrov-Galerkin natural element method securing the numerical integration accuracy. *J. Mech. Sci. Technol.* **2006**, *20*, 94–109. [[CrossRef](#)]
47. Sukumar, N.; Moran, B.; Belytschko, T. The natural element method in solid mechanics. *Int. J. Numer Methods Eng.* **1998**, *43*, 839–887. [[CrossRef](#)]
48. Cho, J.R. Nonlinear free vibration of functionally graded CNT-reinforced composite structures. *Compos. Struct.* **2022**, *281*, 115101. [[CrossRef](#)]
49. Shin, D.K. Large amplitude free vibration behavior of doubly curved shallow open shells with simply-supported edges. *Comput. Struct.* **1997**, *62*, 35–49. [[CrossRef](#)]
50. Shen, S.H.; Xiang, Y. Nonlinear vibration of nanotube-reinforced composite cylindrical panels resting on elastic foundations in thermal environments. *Compos. Struct.* **2014**, *111*, 291–300. [[CrossRef](#)]
51. Kelesdhteri, M.; Jelovica, J. Nonlinear vibration behavior of functionally graded porous cylindrical panels. *Compos. Struct.* **2020**, *239*, 112028. [[CrossRef](#)]
52. Liang, Z.; Gou, J.J.; Zhang, C.; Wang, B.; Kramer, L. Investigation of molecular interactions between (10,10) single-walled nanotube and Epon 862 resin/DETDA curing agent molecules. *Mater. Sci. Eng. A* **2004**, *365*, 228–234. [[CrossRef](#)]
53. Zhu, P.; Lei, Z.X.; Liew, K.M. Static and free vibration analyses of carbon nanotube-reinforced composite plates using finite element method with first order shear deformation plate theory. *Compos. Struct.* **2012**, *94*, 1450–1460. [[CrossRef](#)]
54. Cho, J.R. Large deflection geometrically nonlinear bending of porous nanocomposite cylindrical panels on elastic foundation. *Symmetry* **2024**, *16*, 224. [[CrossRef](#)]

**Disclaimer/Publisher’s Note:** The statements, opinions and data contained in all publications are solely those of the individual author(s) and contributor(s) and not of MDPI and/or the editor(s). MDPI and/or the editor(s) disclaim responsibility for any injury to people or property resulting from any ideas, methods, instructions or products referred to in the content.